Supplementary Material

Orientation-controlled epitaxy of CoSn anisotropic conductive thin films on sapphire substrates toward interconnect applications

Tomoya Nakatani,[1*] Rohit Dahule,[2] Nattamon Suwannaharn,[2] Mevhibe Dilara Pütkül,[1] Yusuke Ikeda,[1] Taisuke T. Sasaki,[2] and Ryoji Sahara,[2]

[1] Research Center for Magnetic and Spintronic Materials, National Institute for Materials Science, 1-2-1, Sengen, Tsukuba, Ibaraki 305-0047, Japan.
[2] Research Center for Structural Materials, National Institute for Materials Science, 1-2-1, Sengen, Tsukuba, Ibaraki 305-0047, Japan.

[*]Corresponding author's email address: nakatani.tomoya@nims.go.jp

1. Sheet resistance evaluation of buffer layer

The CoSn epitaxial films used in this study were grown on sapphire substrates via metallic buffer layers: (from the substrate side) CoFe (2 nm)/Co (2 nm)/Ru (2 nm) for CoSn$(10\bar{1}0)$ and Ti (2 nm)/Ru (4 nm) for CoSn$(11\bar{2}0)$. Therefore, the contribution of these buffer layers to the total sheet resistance (R_s) must be considered when evaluating the resistivity of CoSn films. Following our previous study, the buffer layer's R_s was estimated by measuring the R_s of samples consisting of buffer layer/AgSn (t_{AgSn}) capped with SiN (3 nm). AgSn is an fcc $Ag_{90}Sn_{10}$ (at. %) alloy with a resistivity of ~30 $\mu\Omega$ cm. The details of this method are described in the Supplementary Material of our previous publication.[1]

Figures S1(a) and S1(b) show $1/R_s$ vs. t_{AgSn} plots for CoFe (2 nm)/Co (2 nm)/Ru (2 nm)/AgSn (t_{AgSn}) on MgO(110) and sapphire$(10\bar{1}0)$ substrates buffered with MgO (5 nm), respectively. In these cases, the results were almost identical for the current directions parallel to the *c* axis and *a* axis of Ru. The inverse of the extrapolated intercept at $t_{AgSn} = 0$ corresponds to the R_s of the buffer layers, yielding $R_s^{buffer} = 217^{+52}_{-36}$ Ω/sq.

on the MgO(110) substrate and $R_s^{buffer} = 258^{+76}_{-48}$ Ω/sq. on the sapphire $(10\bar{1}0)$ substrate. The slope of the linear fit corresponds to the resistivity of the AgSn film, as shown in Figs. S1(a) and S1(b).

Figures S1(c) and S1(d) show the average resistivity of the whole film including the buffer layers, $\rho^{ave} = R_s^{whole} \cdot (t_{CoSn} + t_{buffer})$ by open symbols and the resistivity of the CoSn film, $\rho^{CoSn} = t_{CoSn}/(1/R_s^{whole} - 1/R_s^{buffer})$ by closed symbols. R_s^{total} is the sheet resistance of the entire film, and t_{buffer} is the total thickness of the buffer layers (6 nm). For large t_{CoSn}, the difference between ρ^{ave} and ρ^{CoSn} becomes negligible, particularly along the low-resistivity *c* axis. In contrast, a difference of approximately 10 μΩ cm was observed for t_{CoSn} = 10 nm.

Next, the R_s of Ti (2 nm)/Ru (4 nm) buffer layers on a sapphire$(1\bar{1}02)$ substrate was evaluated by the same method, as shown in Fig. S2. In these samples, R_s depended on the current direction. The buffer layers' R_s was 135^{+20}_{-15} Ω/sq. and 169^{+98}_{-45} Ω/sq. along the *c* axis and $[1\bar{1}00]$ of Ru. Along the direction 45° from the *c* axis, R_s was intermediate between these values: 149^{+8}_{-7} Ω/sq, as shown in Fig. S2(c). The observed orientation dependence of R_s is consistent with the resistivity anisotropy of Ru predicted by first-principles calculations.[2] Figure S2(d) shows the average resistivity of the whole films (open symbols) and the resistivity of the CoSn films (closed symbols).

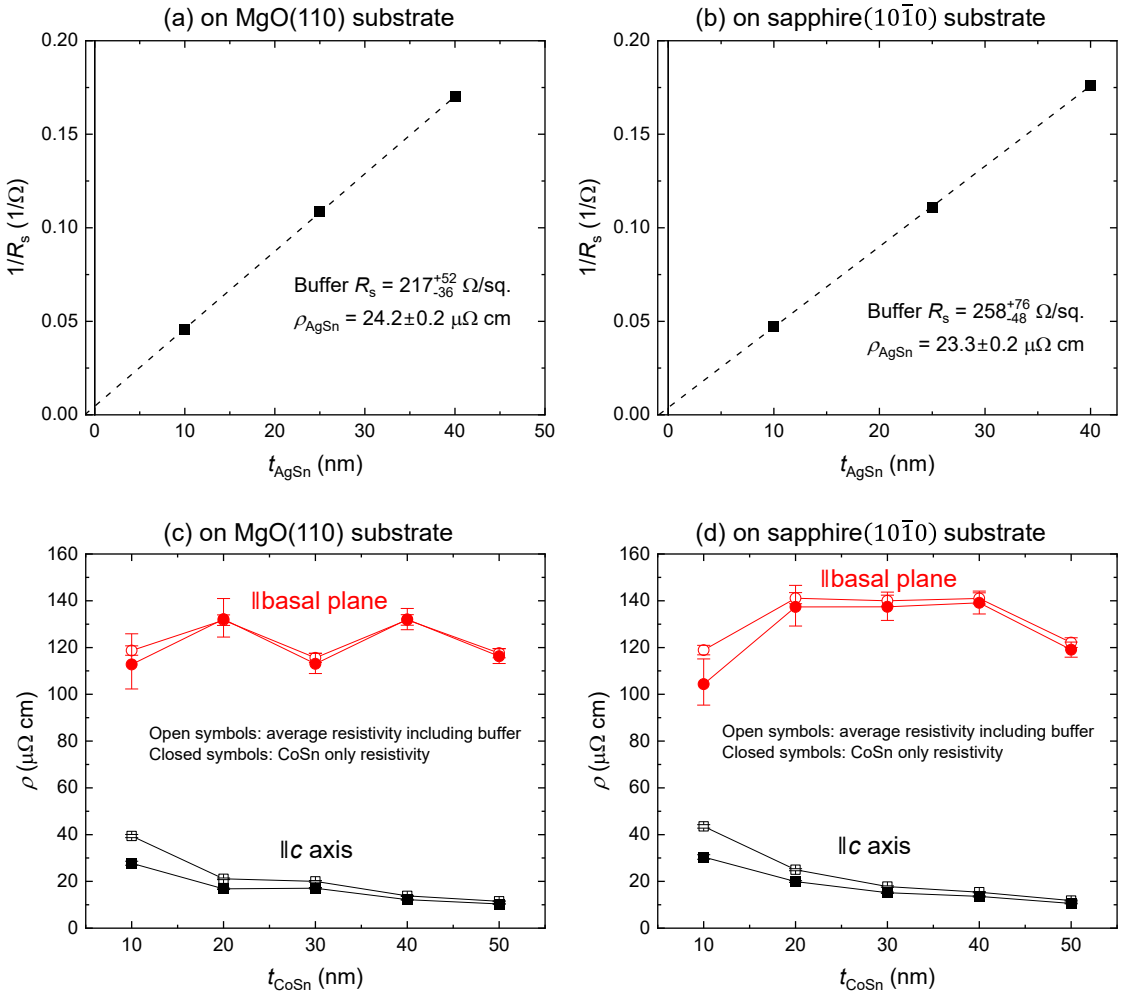


FIG. S1. $1/R_s$ vs. t_{AgSn} plots of CoFe (2 nm)/Co (2 nm)/Ru (2 nm)/AgSn (t_{AgSn}) films deposited on (a) MgO(110) and (b) sapphire $(10\bar{1}0)$ substrates. The $1/R_s$ values extrapolated to $t_{AgSn} = 0$ correspond to R_s of the CoFe (2 nm)/Co (2 nm)/Ru (2 nm) buffer layers. Average resistivity of the whole CoFe/Co/Ru/CoSn films (open symbols) and the resistivity of only the CoSn films (closed symbols) on (c) MgO(110) and (d) sapphire$(10\bar{1}0)$ substrates.

Alt Text: Sheet resistance analysis of CoFe/Co/Ru buffer layers and its effect on the extracted resistivity of CoSn films. Buffer-layer contributions are significant for thin CoSn films and become less important with increasing CoSn thickness.

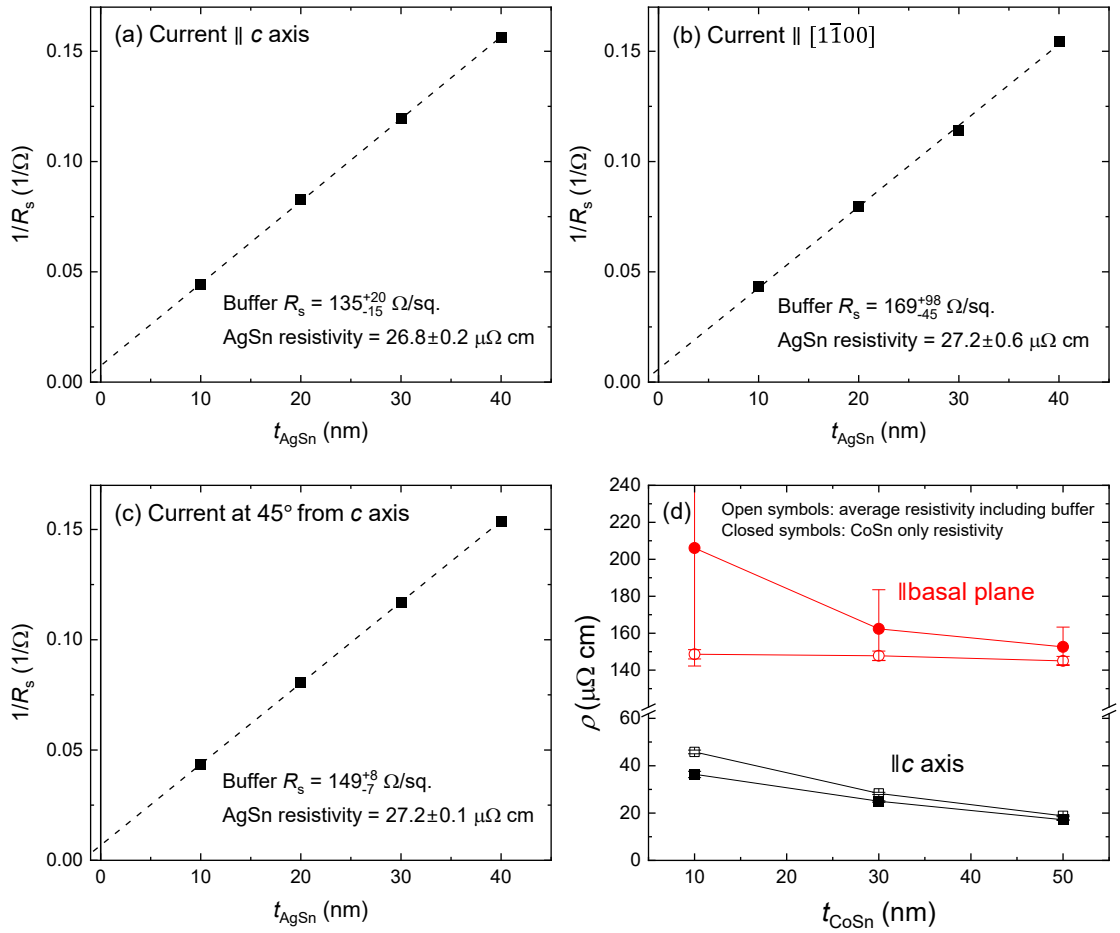


FIG. S2. $1/R_s$ vs. t_{AgSn} plots of Ti (2 nm)/Ru (4 nm)/AgSn (t_{AgSn}) films deposited on a sapphire$(1\bar{1}02)$ substrate for current directions parallel to (a) Ru[0001], (b) Ru$[1\bar{1}00]$, and (c) 45° from Ru[0001]. (d) Average resistivity of the whole Ti/Ru/CoSn films (open symbols) and the resistivity of only the CoSn films (closed symbols).

Alt Text: Sheet resistance analysis of Ti/Ru buffer layers for different current directions. The buffer layers exhibit resistivity anisotropy, and correction of their contribution enables evaluation of the intrinsic resistivity of CoSn films.

2. Chemical states in CoSn films

To examine the oxygen incorporation in the CoSn films, X-ray photoelectron spectroscopy (XPS) was measured for a 50-nm-thick CoSn $(10\bar{1}0)$ films using QuanteraSXM (Ulvac Phi). Figure S3 shows the depth-dependent XPS spectra from Co 2p, Sn 3d, and O 1s. Co-O, Sn-O, and O peak were observed only in the near-surface region of the film, indicating the formation of a surface oxide layer, as confirmed by the STEM observation (Fig. 4). After removal of the surface oxide layer by Ar sputtering etching, no detectable oxygen signal was detected in the film interior.

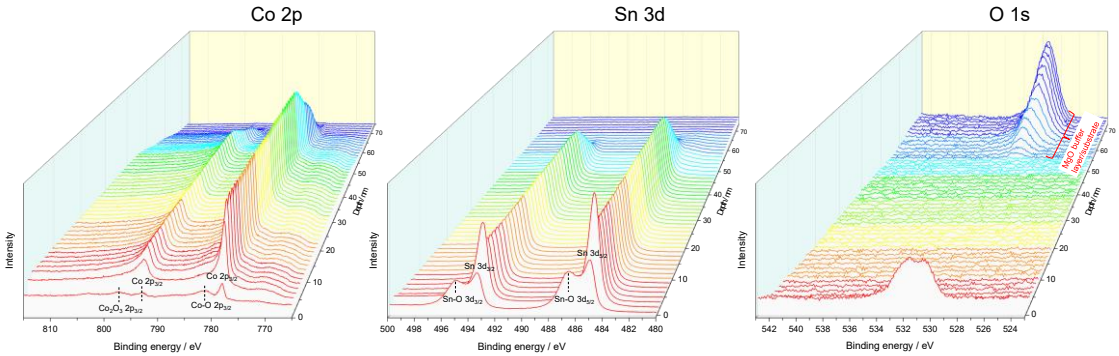


FIG. S3. Depth-dependent XPS spectra of the CoSn 50-nm-thick film for Co 2p, Sn 3d, and O 1s core-levels. "Co-O" can be either CoO and Co_2O_3, and "Sn-O" can be either SnO and SnO_2.

Alt Text: Depth-dependent XPS spectra of a CoSn film. Oxygen-related signals are observed only near the surface, indicating formation of a surface oxide layer without detectable oxygen incorporation in the film interior.

3. DFT calculations of CoSn surface energy

a. Structural relaxation

Figure S4 shows the unrelaxed and relaxed slab geometries of each plane. Upon cleavage, structural relaxation partially compensates for the loss of coordination at the surface. The (0001), (0002), $(10\bar{1}0)$, $(20\bar{2}0)$, and $(11\bar{2}0)$ surfaces undergo relatively modest atomic rearrangements, with relaxation energies ranging from –0.009 to –0.001

eV Å^{-2}. For the (0001) and (0002) surfaces, relaxation is dominated by vertical displacements of the outermost atoms (0.03–0.25 Å) along the surface normal, while in-plane displacements remain negligible. The $(10\bar{1}0)$, $(20\bar{2}0)$, and $(11\bar{2}0)$ surfaces display similar behavior, characterized by vertical displacements of 0.03–0.19 Å along with a small lateral shift of 0.03–0.09 Å. In contrast, the $(22\bar{4}0)$ surface exhibits a stronger, predominantly vertical relaxation, in which the top-layer Co atom shifts inward by 0.27 Å toward the subsurface Sn layer, while the corresponding surface Sn atom moves outward toward the vacuum by 0.25 Å. This results in the largest relaxation energy contribution (–0.017 eV Å^{-2}) among the studied surfaces. Atomic displacements decrease rapidly below the top layer, confirming that both structural and electronic effects are highly localized at the surface. Nevertheless, the cleavage contribution remains the dominant factor determining the total surface energy, and the relative surface stability follows the sequence (0001) < $(20\bar{2}0)$ < (0002) < $(10\bar{1}0)$ < $(22\bar{4}0)$ < $(11\bar{2}0)$.

b. Bader charge analysis

The electronic response to surface relaxation was further examined using Bader charge analysis,[3] and the resulting charge variations are summarized in Table S1. Here, ΔQ is defined as the difference between relaxed and unrelaxed slabs ($\Delta Q = Q_{\text{relaxed}} - Q_{\text{unrelaxed}}$). ΔQ_{layer} and $\Delta Q_{\text{surface}}$ denote the average charge changes in the outermost layer and the exposed surface atoms, respectively. The magnitude of charge redistribution within the outermost layer remains small for all investigated orientations ($|\Delta Q| \leq 0.036$ e), indicating that relaxation induces only localized electronic adjustments. The (0001), (0002), $(10\bar{1}0)$, $(20\bar{2}0)$, and $(11\bar{2}0)$ surfaces show minimal changes, whereas the $(22\bar{4}0)$ surface exhibits the largest charge redistribution at the exposed surface atoms (+0.247 e), consistent with its larger relaxation energy and more pronounced atomic displacements. The correlation between relaxation energy and charge redistribution suggests a coupling between structural relaxation and electronic reconstruction at the surface. The $(22\bar{4}0)$ surface shows larger relaxation and enhanced charge redistribution, indicating a less favorable atomic coordination at the surface and a stronger tendency toward surface roughening.[4] Among the two experimentally observed orientations, the CoSn$(10\bar{1}0)$ surface is substantially more stable than the CoSn$(11\bar{2}0)$ surface. This difference in

surface stability is consistent with the experimentally observed morphology evolution.

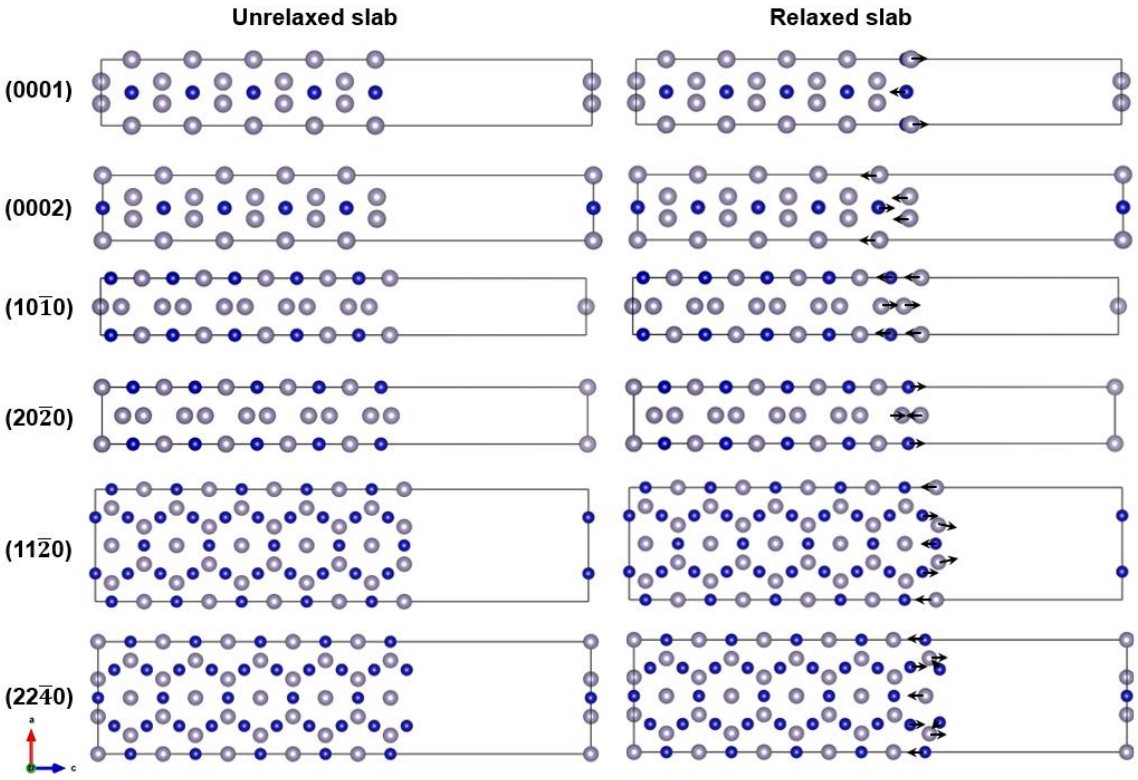


FIG. S4. Unrelaxed and relaxed slab geometries for the CoSn (0001), (0002), (10$\bar{1}$0), (20$\bar{2}$0), (11$\bar{2}$0), and (22$\bar{4}$0) surfaces. Co and Sn atoms are shown in blue and gray, respectively. Arrows denote atomic displacements induced by structural relaxation.

Alt Text: Unrelaxed and relaxed atomic structures of representative CoSn surfaces. Surface relaxation is generally localized near the surface, with the largest structural rearrangement occurring for the (22$\bar{4}$0) surface.

Table S1. Bader charge redistribution in the outermost layer and exposed atoms of CoSn surfaces.

Alt Text: Bader charge redistribution associated with relaxation of CoSn surfaces. Most surfaces exhibit only small charge redistribution, whereas the $(22\bar{4}0$ surface shows a substantially larger electronic reconstruction.

Surface	Number of atoms in layer (surface)	ΔQ_{layer} (e)	$\Delta Q_{\text{surface}}$ (e)
(0001)	6 (4)	-0.035	-0.030
(0002)	6 (2)	0.026	-0.011
$(10\bar{1}0)$	6 (2)	-0.036	0.007
$(20\bar{2}0)$	6 (4)	-0.033	-0.011
$(11\bar{2}0)$	12 (4)	-0.022	-0.032
$(22\bar{4}0)$	12 (2)	-0.021	0.247

References

[1] T. Nakatani, N. Suwannaharn, and T.T. Sasaki, "Fabrication and characterization of single-crystalline CoSn($101^{-}0$) kagome metal thin films for interconnect applications: Structure and anisotropic electrical resistivity," Appl. Phys. Lett. **127**(20), 203302 (2025).

[2] E. Milosevic, S. Kerdsongpanya, A. Zangiabadi, K. Barmak, K.R. Coffey, and D. Gall, "Resistivity size effect in epitaxial Ru(0001) layers," J. Appl. Phys. **124**(16), 165105 (2018).

[3] G. Henkelman, A. Arnaldsson, and H. Jónsson, "A fast and robust algorithm for Bader decomposition of charge density," Comput. Mater. Sci. **36**(3), 354–360 (2006).

[4] M. Methfessel, D. Hennig, and M. Scheffler, "Trends of the surface relaxations, surface energies, and work functions of the 4*d* transition metals," Phys. Rev. B **46**(8), 4816 (1992).